Formation mechanism and the role of nanoparticles in Fe-Cr ODS steels developed for radiation tolerance

Luke L. Hsiung,[1,*] Michael J. Fluss,[1] Scott J. Tumey,[1] B. William Choi,[1] Yves Serruys,[2] Francois Willaime,[2] and Akihiko Kimura[3]

[1]*Physical and Life Sciences Directorate, Lawrence Livermore National Laboratory, Livermore, California 94551, USA*

[2]*Service de Recherches de Métallurgie Physique, CEA, Gif-sur-Yvette 91191, France*

[3]*Institute of Advanced Energy, Kyoto University, Gokasho, Uji, Kyoto 611-0011, Japan*

(Received 27 September 2010; revised manuscript received 5 October 2010; published 9 November 2010)

Structures of nanoparticles in Fe-16Cr-4.5Al-0.3Ti-2W-0.37Y_2O_3 (K3) and Fe-20Cr-4.5Al-0.34Ti-0.5Y_2O_3 (MA956) oxide dispersion strengthened (ODS) ferritic steels produced by mechanical alloying (MA) and followed by hot extrusion have been studied using high-resolution transmission electron microscopy (HRTEM) techniques to understand the formation mechanism of nanoparticles in MA/ODS steels. The observations of Y-Al-O complex-oxide nanoparticles in both ODS steels imply that decomposition of Y_2O_3 in association with internal oxidation of Al occurred during mechanical alloying. While the majority of oxide nanoparticles formed in both steels is $Y_4Al_2O_9$, a few oxide particles of $YAlO_3$ are also observed occasionally. These results reveal that Ti (0.3 wt %) plays an insignificant role in forming oxide nanoparticles in the presence of Al (4.5 wt %). HRTEM observations of crystalline nanoparticles larger than ~2 nm and amorphous or disordered cluster domains smaller than ~2 nm provide an insight into the formation mechanism of oxide nanoparticle in MA/ODS steels, which we believe from our observations involves solid-state amorphization and recrystallization. The role of nanoparticles in suppressing radiation-induced swelling is revealed through TEM examinations of cavity distributions in ion-irradiated Fe-14Cr and K3-ODS ferritic steels. HRTEM observations of helium-filled cavities (helium bubbles) preferably trapped at nanoscale oxide particles and clusters in ion-irradiated K3-ODS are presented.

DOI: 10.1103/PhysRevB.82.184103 PACS number(s): 68.37.Og, 46.70.−p, 61.46.Df, 61.80.−x

I. INTRODUCTION

One of the major challenges in designing future fusion reactors is to develop the high-performance structural materials for first wall and diverter components, which will be exposed high-energy neutrons (14 MeV) from the deuterium-tritium fusion and helium (He) and hydrogen (H) from in (α,n)- and (n,p)-transmutation reactions.[1] The choice of structural materials dictates the design of the fusion reactor systems. In particular, the allowable power plant operating temperature, the choice of coolant, and the power conversion system are critically dependent on the performance characteristics of the materials. The selection of suitable structural materials is based on conventional properties (such as thermophysical, mechanical, and corrosion and compatibility), low neutron-induced radioactivity, and resistance to radiation-induced damage phenomena such as material hardening/embrittlement and/or dimensional instability caused by void- and helium-driven swelling.[1,2] Oxide dispersion strengthened (ODS) steels, which produced by mechanical alloying (MA) of the elemental (or prealloyed) metallic powder with yttria (Y_2O_3) oxide powder and consolidated by hot extrusion or hot isostatic pressing, are a class of advanced structural materials with a potential to be used at elevated temperatures due to the dispersion of thermally stable oxide nanoparticles into the matrix. ODS steels are resistant to radiation-induced swelling and have improved creep strength and oxidation/corrosion resistance at elevated temperatures compared to conventional steels. Thus an operating temperature of the first wall in future fusion of >700 °C (Ref. 3) is possible, resulting in an improved efficiency of ≥40%.[4]

Although significant progress has been made recently on the processing-microstructure-property relationships of ODS steels, see reviews of the subject in the literature,[5,6] it remains to understand the role of fusion-relevant helium and hydrogen transmutation gases on the deformation, fracture, and cavitational swelling of ODS steels. Since no prototype fusion reactors currently exist, it is difficult to directly evaluate the effects of high-energy neutron and transmutation gases on the first wall and diverter components of a fusion reactor. One technique commonly used to study the evolution of defect structures and the kinetics of cavity formation utilizes transmission electron microscopy (TEM) examinations of specimens simultaneously bombarded by heavy ions and helium and/or deuterium ions through so-called "dual-beam" and/or "triple-beam" accelerated experiments.[7] The heavy ions create atomic displacements while the gas ions result in the effects of the transmutation gases, helium (10 appm/dpa) and hydrogen (40–45 appm/dpa).[1,8] In preparation for the dual-beam and triple-beam experiments, we have conducted high-resolution TEM (HRTEM) characterization of as-fabricated Fe-16Cr and Fe-20Cr ODS steels with alloying additions of Al and Ti to document crystal structure, density population, size distribution, and interfacial structure of oxide nanoparticles. Emphasis was placed on studying the formation mechanism of nanoparticles that are crucial in trapping helium bubbles to suppress radiation-induced cavitational swelling.

II. EXPERIMENTAL

The ODS steels used for this investigation were Fe-16Cr-4Al-2W-0.3Ti-0.3Y_2O_3 [designated as K3 (Ref. 9)]

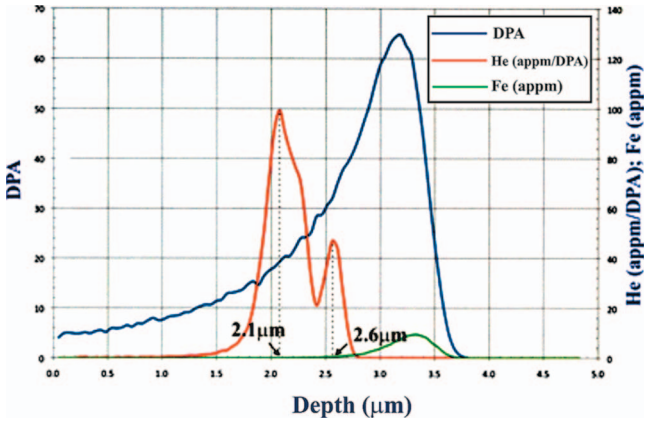

FIG. 1. (Color) TRIM calculation of dose (dpa), helium-to-dpa ratio (appm/dpa), and Fe (appm) profiles. The penetration depth of ions was over a region that extends from 1.5 to 2.75 μm beneath the specimen surface for He and extends from 2.75 to 3.6 μm beneath the specimen surface for Fe.

ODS ferritic steels and Fe-20Cr-4.5Al-0.34Ti-0.5Y_2O_3 [designated as MA956 (Ref. 10)]. A full description of the fabrication procedure for the ODS steels can be found elsewhere.[11,12] Briefly, the prealloyed powder was first mechanically alloyed with Y_2O_3 powder in an argon gas atmosphere at room temperature using an attrition-type ball mill. The powder was then sealed in a stainless steel can and degassed at 400 °C in 0.1 Pa pressure. The canned powders were subsequently consolidated by a hot extrusion technique at 1150 °C for K3-ODS and 1107 °C for MA956-ODS steel. After the extrusion, the consolidated K3-ODS steel was thermally treated at 1050 °C for 1 h. One sample of K3-ODS steel was also annealed at 900 °C for 168 h (1 week) for a thermal-stability study. The chemical composition (in weight percent) of the two ODS steels are: C: 0.08, Si: 0.033, Cr: 16, W: 1.82, Al: 4.59, Ti: 0.28, Y_2O_3:0.368, and Fe: balance for K3-ODS steel,[9] and Cr: 20, Al: 4.5, Ti: 0.34, Y_2O_3:0.5, and Fe: balance for MA956-ODS steel.[10] For the purpose of investigating the role of nanoparticles in radiation tolerance of ODS steels, a non-ODS Fe-14 wt % Cr alloy was also prepared using a vacuum arc-melting method followed by hot rolling at 1050 °C. Dual-beam irradiation of Fe-14Cr alloy and K3-ODS steel loaded in a stainless-steel specimen holder using 24.18 MeV Fe^{8+} ions for displacement damage and energy-degraded 1.7 MeV He^+ ions for helium injection was conducted at the JANNUS facility, Saclay, France. The irradiation temperature was controlled at 425 ± 5 °C using a proportional-integral-derivative referenced thermocouple located on the specimen holder. The specimen temperature uniformity was estimated by monitoring the surface temperature of the specimen using a digital infrared camera during heating and ion irradiation. The surface temperature was uniform within ±2.5 °C and tracked well with the controlling thermocouple. Figure 1 shows the calculated profiles of displacement damage in dpa (displacement per atom), Fe^{8+}, and He^+ using TRIM code. The implantation depth of helium was over a region extending from 1.5 to 2.75 μm beneath the specimen surface to avoid overlapping with the Fe^{8+} ion region that was over a region extending from 2.75 to 3.6 μm beneath the specimen surface. The displacement damage at the peak position was 65 dpa and the specimens were irradiated at $\sim 1\times10^{-3}$ dpa/s. The nominal conditions for ion irradiation at the helium implantation region are as follows: the displacement damage gradually increases from 10 dpa (at 1.5 μm) to 40 dpa (at 2.75 μm), and there are two peaks for helium to dpa ratio within the helium implantation region: 100 appm/dpa at 2.1 μm and 25 appm/dpa at 2.6 μm.

Thin foils of the as-fabricated ODS steels for TEM examination were prepared by a standard procedure that includes slicing, grinding, and polishing. Final thinning of the foils was performed using a standard twin-jet electropolishing technique in an electrolyte (90 vol % acetic acid, 10 vol % perchloric acid) at 30 V and room temperature. Cross-section TEM foils (10 μm × 6 μm × < 0.1 μm) of irradiated Fe-14Cr and K3-ODS were prepared using a focused ion-beam method. The foils were lifted out using a micropickup system and mounted onto a copper grid. TEM characterizations were performed using a Phillips CM300 field-emission transmission electron microscope (accelerating voltage of 300 kV). A software package CARINE CRYSTALLOGRAPHY 3.1 (Ref. 13) was used to simulate electron-diffraction patterns to identify the crystal structure of oxide nanoparticles.

III. RESULTS AND DISCUSSION

Typical microstructures of K3 and MA956 ODS steels are shown in Figs. 2(a) and 1(b) and Figs. 2(c) and 2(d), respectively. Here elongated grains and oxide nanoparticles, mainly $Y_4Al_2O_9$ (YAM: yttrium aluminum monoclinic) were observed in both of these ODS steels. However, the oxide nanoparticle density for MA956-ODS is much lower than that for K3-ODS. The number density and size distribution of oxide particles of both ODS steels were investigated using energy-filtered TEM (EFTEM) method. The results are shown in Figs. 3 and 4 for K3-ODS and MA956-ODS, respectively. The nanoparticle sizes in K3-ODS are typically ranging from 1.69 to 67.24 nm in diameter with a mean particle size: 5.91 nm and a particle density: 1.33×10^{22} m^{-3}, whereas the nanoparticle sizes in MA956-ODS are typically ranging from 2.15 to 79.4 nm in diameter with the mean particle size: 8.07 nm and a particle density: 1.0×10^{20} m^{-3}. It is worth noting that these results may also indicate that the size limit of observable nanoparticles using energy-filtered electron microscopy is 1.7 nm. As we will demonstrate below, the smallest crystalline nanoparticles we observed by HRTEM are in the range of 1.7–2 nm. Particles or cluster domains smaller than this, in our observations, were featureless or possibly amorphous in nature and were difficult to resolve using conventional TEM imaging techniques.

The formation of $Y_4Al_2O_9$ oxide nanoparticles in both ODS steels was identified and confirmed by matching observed and simulated diffraction patterns, an example of which is shown in Fig. 5 for the $[432]_{YAM}$-zone diffraction pattern. $Y_4Al_2O_3$ (YAM) has a monoclinic structure (space group: $P2_1/c$) with lattice parameters: a=0.7375 nm, b

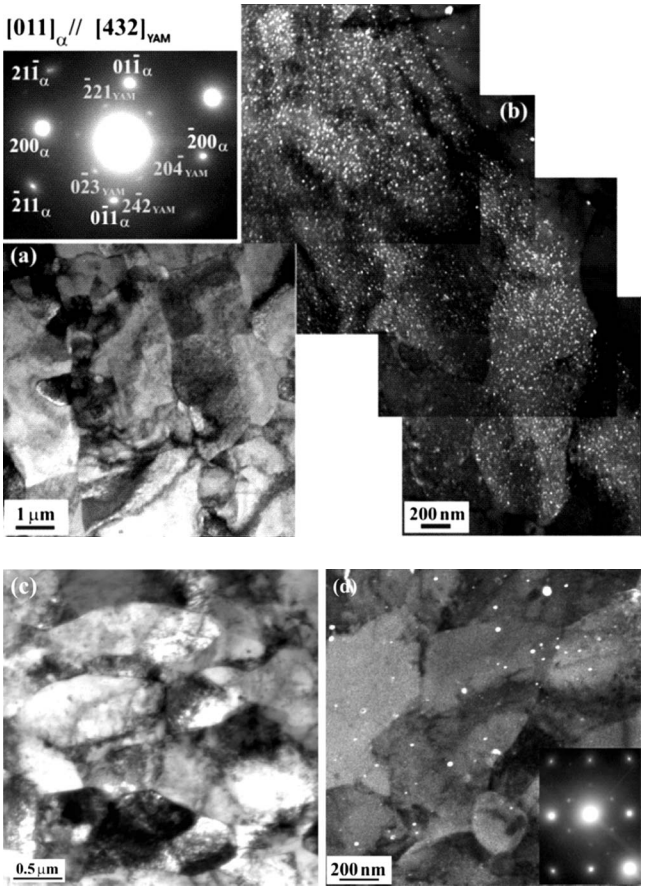

FIG. 2. (a) Bright-field TEM image shows typical grain morphology of K3-ODS steel, (b) dark-field TEM image and selected-area diffraction pattern of the $[011]_{\text{Fe-Cr}(\alpha)}\|[432]_{\text{YAM}}$ zone show the formation of dense $Y_4Al_2O_9$ nanoparticles in K3-ODS steel, (c) bright-field TEM image shows typical grain morphology of MA956-ODS steel, and (d) dark-field TEM image and selected-area diffraction pattern of the $[011]_{\text{Fe-Cr}(\alpha)}\|[432]_{\text{YAM}}$ zone show the formation of $Y_4Al_2O_9$ nanoparticles in MA956-ODS steel.

$=1.0507$ nm, $c=1.1113$ nm, and $\beta=108.58°$.[14,15] An orientation relationship between the $Y_4Al_2O_9$ oxide nanoparticle and the Fe-Cr (α) matrix can be derived from the diffraction pattern: $(0\bar{1}1)_\alpha\|(2\bar{4}2)_{\text{YAM}}$ and $[011]_\alpha\|[432]_{\text{YAM}}$. By comparing the $Y_4Al_2O_9$ nanoparticles formed in the ODS steel

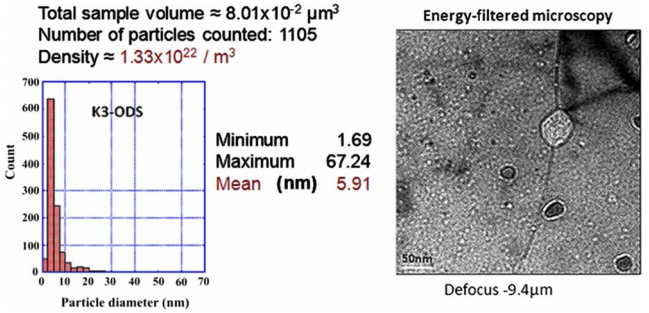

FIG. 3. (Color online) The number density, the size distribution, and the mean size of oxide particles in K3-ODS steel are displayed together with a typical morphology of nanoparticles observed using energy-filtered microscopy.

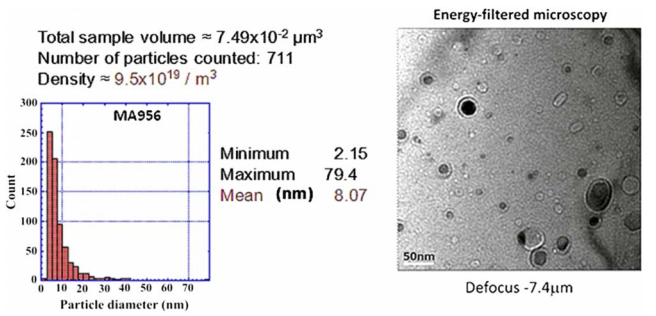

FIG. 4. (Color online) The number density, the size distribution, and the mean size of oxide particles in MA956-ODS steel are displayed together with a typical morphology of nanoparticles observed using energy-filtered microscopy.

with the starting Y_2O_3 particles [space group: Ia_3, a cubic structure with $a_o=1.06$ nm,[14] particle size distribution: 15–50 nm (Ref. 16)] used to fabricate the ODS steels, we can realize that the formation of oxide nanoparticles in ODS steels is not solely through fragmentation of Y_2O_3 particles. In fact, a more complex formation mechanism, which involves fragmentation of Y_2O_3 particles, decomposition/dissolution of Y_2O_3 fragments, and reprecipitation of nanoscale precipitates/clusters, has been proposed by Okuda and Fujiwara,[17] Kimura *et al.*,[18] Sakasegawa *et al.*,[19] and Alinger *et al.*[20] To form $Y_4Al_2O_9$ nanoparticles in consolidated MA/ODS steels, the following three reactions should also take place: (1) a dissolution of Y_2O_3 powder particles: $Y_2O_3 \rightarrow 2[Y]+3[O]$, (2) an internal oxidation reaction of Al: $2[Al]+3[O]\rightarrow Al_2O_3$ due to the higher oxygen affinity of

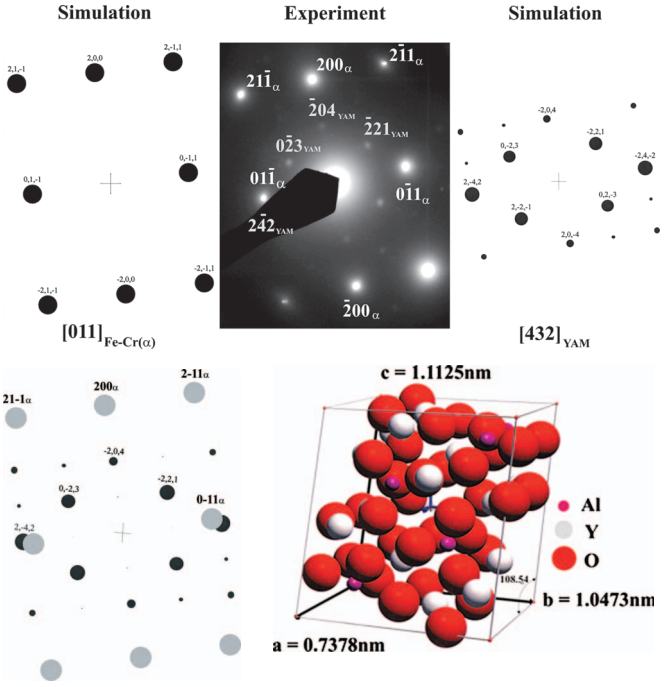

FIG. 5. (Color) (a) Observed and simulated diffraction patterns of the $[011]_{\text{Fe-Cr}(\alpha)}$ zone and the $[432]_{\text{YAM}}$ zone for identifying the formation of $Y_4Al_2O_9$ complex-oxide nanoparticles; (b) superimpose of the simulated $[011]_{\text{Fe-Cr}(\alpha)}$-zone and $[432]_{\text{YAM}}$-zone patterns; and (c) crystal structure of $Y_4Al_2O_9$ oxide compound.

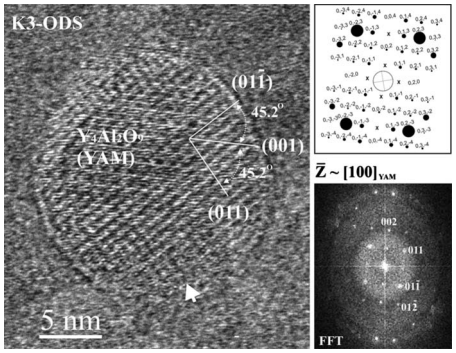

FIG. 6. HRTEM and FFT images of a large $Y_4Al_2O_9$ (>20 nm) nanoparticle obtained at a defocus condition of −20 nm. A simulated diffraction pattern of the $[100]_{YAM}$ zone is displayed.

Al [i.e., Al>Ti>Cr>Fe (Ref. 21)], and (3) a complex-oxide formation reaction: $2Y_2O_3+Al_2O_3 \rightarrow Y_4Al_2O_9$, which can take place at temperatures between 900 and 1100 °C.[22] Most recent studies of oxide nanoparticles in various ODS steels conducted by Marquis[23] using atom probe tomography (APT), Klimenkov *et al.*[24] using energy dispersive x-ray (EDX) and electron-energy-loss spectroscopy, and Hsiung *et al.*[25] using HRTEM revealed the existence of a core/shell structure in oxide nanoparticles. The findings of core/shell structures in oxide nanoparticles therefore suggest that the dissolution/reprecipitation mechanism previously proposed for the formation of oxide nanoparticles in as-fabricated ODS steels is not fully accountable. More HRTEM results obtained from K3 and MA956 ODS steels are reported here in order to clarify the formation mechanism of oxide nanoparticles in MA/ODS steels.

A. HRTEM structure of oxide nanoparticles in K3 and MA956 ODS steels

1. K3-ODS steel

HRTEM studies of the structure of oxide nanoparticles and the orientation relationships between the oxide nanoparticle and the matrix were mainly conducted from K3-ODS steel samples. Since the majority of oxide nanoparticles in K3-ODS steel has a size (diameter) ranging from 1.7 to 30 nm according to the size distribution of oxide particles shown in Fig. 3, more attention was paid on nanoparticles smaller than 30 nm. More than one hundred oxide nanoparticles (mostly $Y_4Al_2O_9$) were imaged and analyzed; some noteworthy results are reported here.

Figures 6 and 7 show HRTEM images obtained from a large oxide nanoparticle (20 nm in diameter) under three different defocus conditions. This large nanoparticle, which is identified to be $Y_4Al_2O_9$ according to the fast Fourier transformation (FFT) image and the simulated $[100]_{YAM}$-zone pattern, is nearly spherical and incoherent with the matrix. Notice that the lower portion of the large nanoparticle contains a disordered (amorphous) domain, which does not exhibit any lattice fringes as those that appeared on the upper portion of the particle. Apparently, this large nanoparticle is only partially crystallized, and its structure is described by a central crystalline core and an amorphous shell. On the other hand, small nanoparticles (<10 nm in diameter), as shown in Figs. 8 and 9, tend to have a facetted shape and are coherent or semicoherent with the matrix. The FFT image generated from the nanoparticle in Fig. 8 is of the $[100]_{YAM}$ zone that is in agreement with the simulated $[100]_{YAM}$-zone pattern. An orientation relationship between the nanoparticle and the matrix derived from the FFT image is: $(0\bar{1}1)_\alpha \| (004)_{YAM}$ and $[011]_\alpha \| [100]_{YAM}$. The FFT image generated from the nanoparticle in Fig. 9 is of the $[012]_{YAM}$ zone that is in agreement with the simulated $[012]_{YAM}$-zone pattern. An orientation relationship between the nanoparticle and the matrix derived from the FFT image is: $(0\bar{1}1)_\alpha \| (2\bar{4}2)_{YAM}$ and $[011]_\alpha \| [012]_{YAM}$. Clearly, both nanoparticles are fully crystallized $Y_4Al_2O_9$; each has an orientation relationship with the matrix that is different from the one shown in Fig. 5. A relative larger coherent strain, $\Delta\epsilon = \left|1-\frac{(d_{004})_{YAM}}{(d_{0\bar{1}1})_\alpha}\right| = 30\%$, is evaluated for the nanoparticle in Fig. 8 compared to a coherent strain, $\Delta\epsilon = \left|1-\frac{(d_{2\bar{4}2})_{YAM}}{(d_{0\bar{1}1})_\alpha}\right| = 9.9\%$, evaluated for the nanoparticle in Fig. 9. We note that inserting misfit dislocations at the interfaces to form semicoherent interfaces can reduce the coherent strains.

Figure 10 shows a partially crystallized oxide nanoparticle (~7 nm in diameter) that contains a crystalline

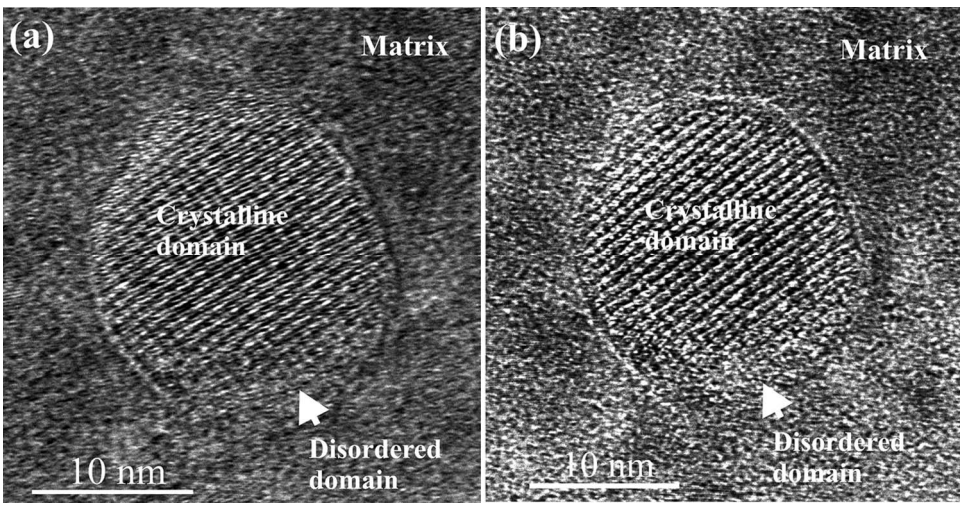

FIG. 7. HRTEM images of the same $Y_4Al_2O_9$ nanoparticle in Fig. 6 obtained at two different defocus conditions (a) −50 nm and (b) −75 nm.

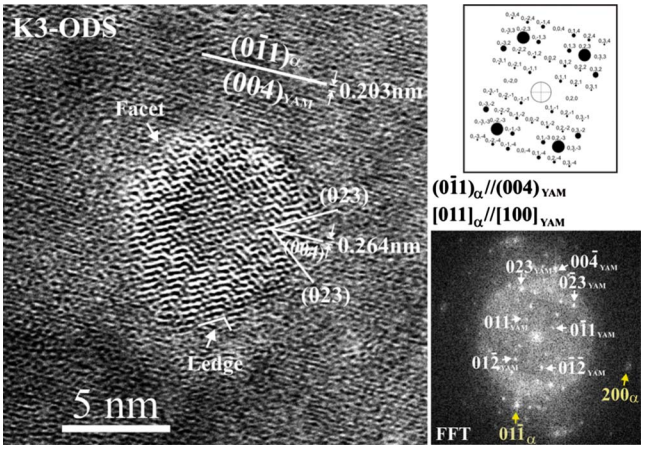

FIG. 8. (Color online) HRTEM image shows a facetted small nanoparticle. The orientation relationship between the oxide nanoparticle and the matrix can be derived from the FFT image.

$Y_4Al_2O_9$ domain (2 nm × 5 nm in dimension). The FFT image generated from the crystalline $Y_4Al_2O_9$ domain is of the $[432]_{YAM}$ zone that is in agreement with the simulated $[432]_{YAM}$-zone pattern. An orientation relationship between the crystalline $Y_4Al_2O_9$ domain and the matrix is $(0\bar{1}1)_\alpha \| (2\bar{4}2)_{YAM}$ and $[011]_\alpha \| [432]_{YAM}$, which is the same as the one shown in Fig. 6. HRTEM observation of the interfacial structure between the crystalline $Y_4Al_2O_9$ domain and the matrix, as shown in Fig. 11(a), reveals facets, ledges, and remnant (thin shell) of amorphous domains at the interface. Figure 11(b) shows the high-magnification view of an amorphous domain in the specified area in Fig. 11(a). These observations together with the observations shown in Figs. 6 and 7 clearly reveal that a solid-state amorphization of oxide nanoparticles has taken place during the MA of the ODS steel. Figure 12 shows another important feature that can only be explained by the crystallization of an amorphous oxide nanoparticle during consolidation. Here two crystalline $Y_4Al_2O_9$ domains, designated as the $[432]_I$ domain and the

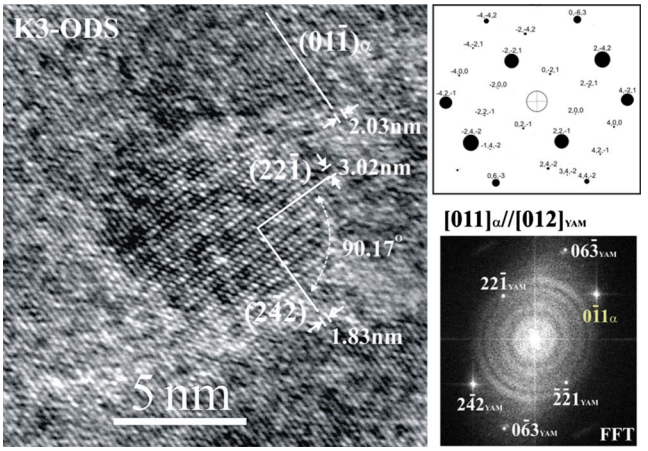

FIG. 9. (Color online) HRTEM image shows a facetted and fully crystallized small nanoparticle ($d < 10$ nm) that is coherent with the matrix. The orientation relationship between the oxide nanoparticle and the matrix can be derived from the FFT image.

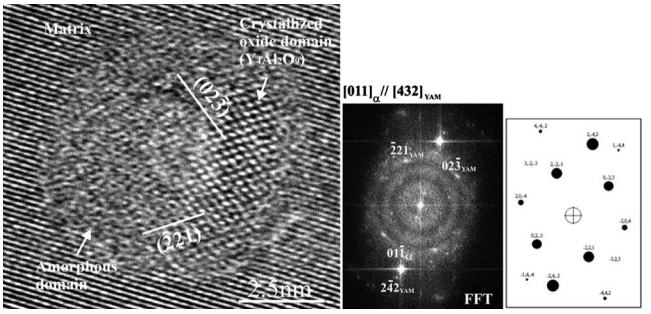

FIG. 10. HRTEM image shows a $Y_4Al_2O_9$ crystalline domain (2 nm × 5 nm) formed in a partially crystallized nanoparticle and a FFT image is displayed with a simulated diffraction pattern of the $[432]_{YAM}$ zone. The orientation relationship between the crystalline domain and the matrix is the same as the one shown in Fig. 6.

$[221]_{II}$ domain, can be identified within a partially crystallized oxide nanoparticle according to the FFT images. While the structure of the left-hand-side interface between the $[432]_I$ domain and the matrix is similar to that shown in Fig. 11, the structure of the right-hand-side interface between the $[221]_{II}$ domain and the matrix is shown in Fig. 13(a), in which facets, ledges, and a remnant (thin shell) of amorphous domains can be readily seen at the interface. Figure 13(b) shows the high-magnification view of an amorphous domain in the specified area in Fig. 13(a). One more orientation relationship between $Y_4Al_2O_9$ and the matrix is found here: $(0\bar{1}1)_\alpha \| (2\bar{3}2)_{YAM}$ and $[011]_\alpha \| [221]_{YAM}$. A coherent strain, $\Delta\epsilon = \left|1 - \frac{(d_{2\bar{3}2})_{YAM}}{(d_{0\bar{1}1})_\alpha}\right| = 2\%$, is evaluated for the right-hand-side interface.

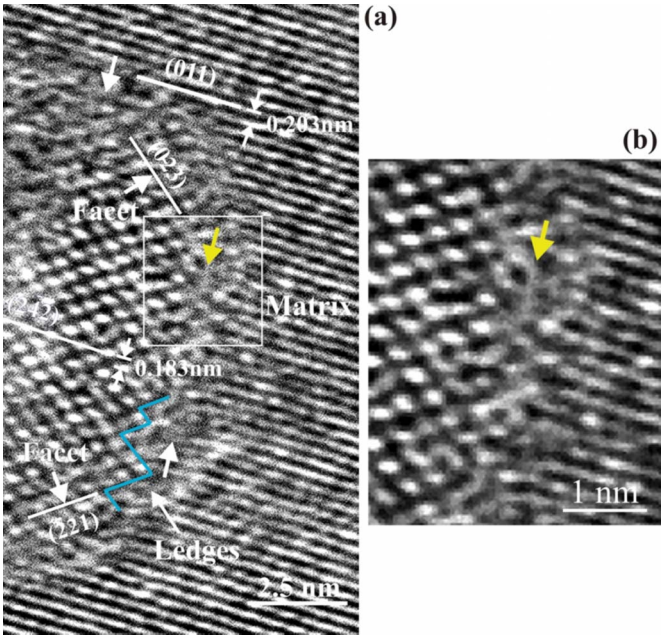

FIG. 11. (Color online) HRTEM images show the structure of interface between the crystalline domain and the matrix in Fig. 9. (a) Facets, ledges, remnant of amorphous domains (marked by arrows) can be readily seen at the interfaces and (b) a higher magnification view of an amorphous domain in a framed area in (a).

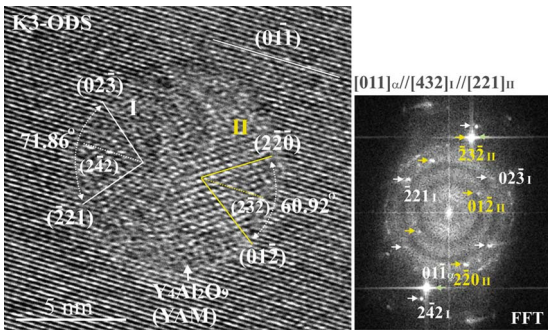

FIG. 12. (Color online) HRTEM image shows the formation of multiple $Y_4Al_2O_9$ domains in an oxide nanoparticle. Two different orientation relationships between $Y_4Al_2O_9$ oxide and the matrix can be readily derived from the FFT image.

Thus, altogether four different orientation relationships have been found between the coherent $Y_4Al_2O_9$ nanoparticles and the matrix. The existence of multiple orientation relationship is likely due the monoclinic structure of $Y_4Al_2O_9$ where the $\{011\}_\alpha$ planes act as habit planes for the formation of $Y_4Al_2O_9$ nanoparticles through a ledge growth mechanism. The formation of core/shell structure in oxide nanoparticles is dependent on the size of nanoparticles; large particles have a thicker shell, and small particles have either a thinner shell or no shell.

Amorphous or disordered cluster domains smaller than 2 nm were observed using HRTEM but could not be detected using EFTEM. The result is shown in Fig. 14, in which the atomic structure of a nearly perfect matrix of the [012] zone is shown in Fig. 14(a), and several amorphous or disordered cluster domains (marked by circles) are shown in Figs. 14(b)–14(d). The featureless appearance of disordered cluster domains can be readily seen in comparison to the lattice-fringe appearance of the [012] crystalline matrix. The observations of crystalline and stoichiometric oxide nanoparticles larger than 2 nm and disordered cluster domains smaller than 2 nm suggest that the crystallization of amorphous or disordered domains during the consolidation of the K3-ODS at 1150 °C cannot take place when the domain sizes are smaller than a critical size ($d_c \approx 2$ nm) due to the insurmountable increase in interfacial energy. To further verify and confirm that the solid-state amorphization of oxide particles does occur during MA of K3-ODS steel, another crucial observation is shown in Fig. 15. Here a $Y_4Al_2O_9$ nanoparticle of the $[311]_{YAM}$ zone, according to the observed FFT image and the simulated $[311]_{YAM}$-zone pattern, is shown in Fig. 15(a). A higher magnification image taken from the lower portion of the nanoparticle (marked by two arrows) is shown in Fig. 15(b). Here the fragmentation of a powder particle presumably occurred through an ablation and/or a cleavage fracture during MA can still be recognized from a remnant of sharp and irregular particle/matrix interface. An amorphous domain (marked by arrows) remains adjacent to the recrystallized fragment, which is no longer Y_2O_3 but $Y_4Al_2O_9$, suggesting that a solid-state amorphization does occur during MA presumably through disordering and solute mixing of Y_2O_3 particle fragments with the matrix constituents (M: Fe, Cr, Al, W, Ti), i.e.,

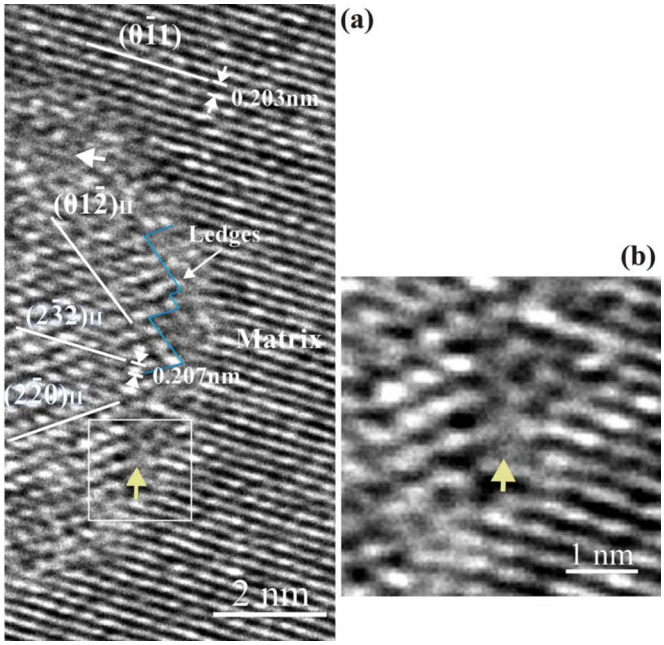

FIG. 13. (Color online) HRTEM image shows the interfacial structure of the nanoparticle in Fig. 12. (a) Facets, ledges, and remnant of amorphous domains (marked by arrows) can be found at the oxide (domain II)/matrix interface and (b) a higher magnification view of an amorphous domain in a framed area in (a).

$$Y_2O_3 + M \xrightarrow{\text{disordering \& solute mixing}} [YMO]_{\text{amorphous}}.$$

We believe that the results shown here strongly support the idea that during the consolidation at 1150 °C, nucleation of the crystalline complex-oxide core occurs within the large amorphous particle ($d > d_c$) by depleting Fe, Cr, W, and Ti to the shell, i.e., $[YMO]_{\text{amorphous}} \xrightarrow{\Delta} Y_4Al_2O_9$ or $YAlO_3$(core) $+M'$(shell). The shell remains amorphous and contains a small amount of oxygen according to the APT analysis reported in Ref. 23. The formation mechanism of amorphous cluster domains ($d < 2$ nm) and oxide nanoparticles ($d > 2$ nm) with a core/shell structure will be further discussed later.

It is noteworthy that the additional alloying elements can enhance amorphization of crystalline materials since the increased number of atom species can render the crystalline materials more difficult to arrange the constituent atoms into crystallized structure; for example, an amorphous phase can be obtained in ball-milled Fe-Cr powder particles in the presence of oxygen, but only a crystalline phase can be obtained in the absence of oxygen.[26] The solid-state amorphization caused by MA has accordingly been employed as one of the nonequilibrium processing routes to produce amorphous materials for many metallic and oxide systems.[27]

2. MA956-ODS steel

HRTEM examinations of oxide nanoparticles in MA956-ODS steel, an early version of Fe-Cr ODS ferritic steel without W addition, were conducted to verify that oxide nanoparticles containing a structure of crystallized core and

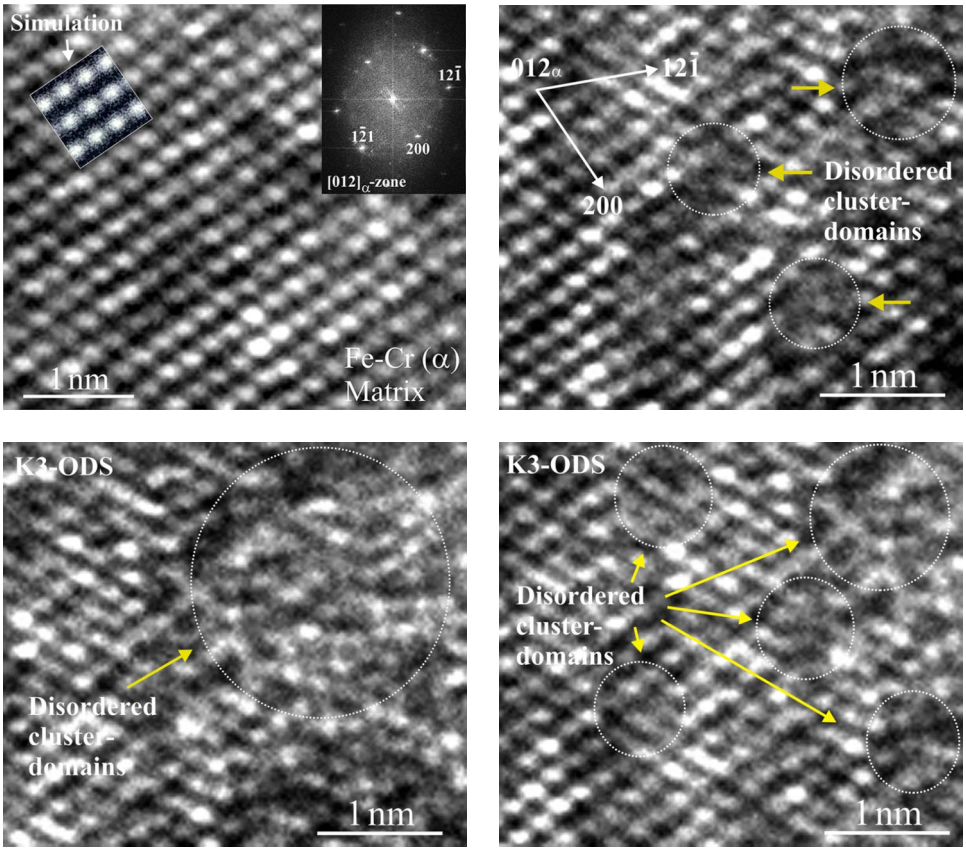

FIG. 14. (Color online) HR-TEM images show the atomic structure of (a) a nearly perfect matrix of the [012] zone and [(b)–(d)] matrices of the [012] zone containing disordered cluster domains ($d<2$ nm). Notice the inset in (a) is the simulated atomic structure of the [012] zone.

amorphous shell can also form in other type of MA/ODS steel. Three large oxide nanoparticles ($d>20$ nm) containing a core/shell structure are shown in Figs. 16(a)–16(c). Here the crystalline cores were identified, according to the FFT images and simulated diffraction patterns, to be $Y_4Al_2O_9$ (YAM) for the nanoparticles shown in Figs. 16(a) and 16(b) and to be $YAlO_3$ (YAP: yttrium aluminum perovskite) for the nanoparticle shown in Fig. 16(c). Notice that the shell is significantly thicker in MA956 than in K3-ODS. The FFT images generated from $Y_4Al_2O_9$ (YAM) cores in Figs. 16(a) and 16(b) are of the $[102]_{YAM}$ zone and of the $[\bar{1}10]_{YAM}$ zone, respectively; the FFT image generated from $YAlO_3$ core in Fig. 16(c) is of the $[212]_{YAP}$ zone. $YAlO_3$ (YAP) has a perovskitelike orthorhombic structure (space group: *Pbnm*) with lattice parameters: $a=0.5179$ nm, $b=0.5329$ nm, and $c=0.737$ nm.[15] YAP can be formed through a complex-oxide formation reaction: $2Y_2O_3+2Al_2O_3 \rightarrow YAlO_3$ at temperatures between 1100 and 1250 °C.[22] Two small ($2<d<3$ nm) and one large ($d\approx 15$ nm) oxide nanoparticles without a core/shell structure are shown in Fig. 17. They were identified to be $Y_4Al_2O_9$ oxide according to the observed FFT image; the large one orients near to the $[102]_I$-zone direction and the two small ones orient near to the $[732]_{II}$-zone direction. Similar to that found in K3-ODS steel, the formation of core/shell structure in MA956-ODS steel is also apparently dependent on the size of the nanoparticles.

The preferred formation of Y-Al-O oxides in K3 and MA956 ODS steels containing both Al (4.5 wt %) and Ti (0.3 wt %) suggests that Ti (0.3 wt %) plays an insignificant role in forming oxide nanoparticles in the presence of Al (4.5 wt %), which is in agreement with the result reported by Kasada *et al.*[10] It is noteworthy that another Y-Al-O oxide compound: $Y_3Al_5O_{12}$ (YAG: yttrium aluminum garnet), which has a cubic structure (space group: *Ia3d*) with a lattice parameter: $a=1.201$ nm, was not observed in as-fabricated K3- and MA-956-ODS steels. That is probably because nanoparticles of $Y_3Al_5O_{12}$ can only be formed through a complex-oxide formation reaction: $3Y_2O_3+5Al_2O_3 \rightarrow 2Y_3Al_5O_{12}$ at temperatures between 1400 and 1600 °C.[22]

B. Formation mechanism of crystalline-oxide nanoparticles and amorphous nanoclusters

Figures 18(a)–18(c) show the result of a K3-ODS steel sample annealed at 900 °C for 168 h. Here a small $Y_4Al_2O_9$ nanoparticle (<10 nm) remains facetted [Fig. 18(a)], a large $Y_4Al_2O_9$ nanoparticle (>20 nm) becomes perfectly spherical without a core/shell structure [Fig. 18(b)], and the mean size and the number density of oxide nanoparticles are 6.6 nm and 1.67×10^{22} cm^{-3}, respectively [Fig. 18(c)], which are about the same values as in the as-fabricated K3-ODS. These results suggest that the core/shell structures of oxide nanoparticles formed in as-fabricated K3 and MA956 ODS steels are in fact far from chemical equilibrium. The formation mechanism of oxide nanoparticles is accordingly proposed and schematically illustrated in Fig. 19(a) based on the above HRTEM observations. The formation mechanism basically include the following stages: (1) fragmentation of starting Y_2O_3 powder particles to form finely dispersed

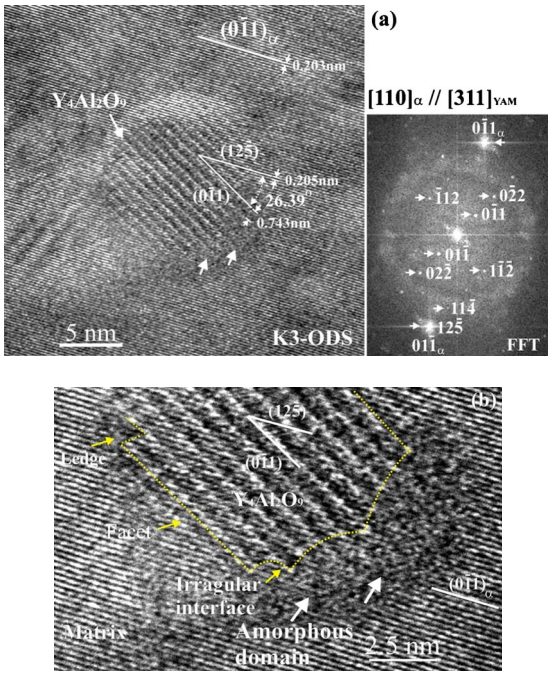

FIG. 15. (Color online) (a) The sharp and irregular particle/matrix interface of a $Y_4Al_2O_9$ nanoparticle of the $[311]_{YAM}$ zone reveals the occurrence of particle fragmentation during MA; (b) a higher magnification image taken from the lower portion of the nanoparticle (marked by arrows) reveals that an amorphous domain (marked by arrows) remains adjacent to the $Y_4Al_2O_9$ fragment. This observation suggests that a solid-state amorphization can occur through the mechanical attrition and chemical agglomeration of Y_2O_3 particles with matrix constituents.

nanoscale fragments during early stages of ball milling; (2) agglomeration and amorphization of fragments mixed with the matrix constituents to form amorphous agglomerates and clusters ([*M*YO], *M*: Fe, Cr, Al, W, and Ti) during later stages of ball milling; (3) crystallization of the amorphous agglomerates larger than a critical size (~2 nm) to form oxide nanoparticles with a complex-oxide core and solute-enriched (*M′*) shell during the consolidation at 1150 °C. It is noteworthy that the fragmentation of oxide particles is more severe at early stages of ball milling; however, the fragmentation is expected to proceed even at later stages of ball milling.

The contents of complex-oxide core and solute-enriched shell are dependent on the compositions of different ODS steels. Y-Al complex-oxide (such as $Y_4Al_2O_9$ and $YAlO_3$) cores can form in Al-contained K3 and MA956 ODS steels, Y-Ti complex-oxide (such as Y_2TiO_5 and $Y_2Ti_2O_7$) cores can form in Ti-contained MA957 ODS steels with no addition of Al,[23] and Y_2O_3 cores can form in Eurofer 9Cr-ODS steels with no additions of Al and Ti.[24] The solute-enriched shells can be perceived as a result of the depletion of the solutes that are not involved in the internal oxidation reactions for the complex-oxide cores such as Cr-enriched shells in the nanoparticles of MA957 and Mn- and V-enriched shells in the nanoparticles of Eurofer 9Cr-ODS steel.[23,24] The shell thickness is dependent on the size of nanoparticles since the larger the particle the more matrix material can be solution mixed during the agglomeration and amorphization stage and thus more solutes will be depleted from the oxide core during the crystallization stage, as illustrated in Fig. 19(b). A solute-enriched shell forms when solute depletion rate from the core is greater than solute diffusion rate from the oxide/matrix interface during the crystallization stage.

C. Nature of cavities in (Fe^{8+}+He^+) dual-ion irradiated Fe-14Cr and K3-ODS

Under steady-state conditions, the radial growth rate of helium-filled cavities is determined by both the excess vacancy flux (*S*) and the helium gas pressure (P_g) from the

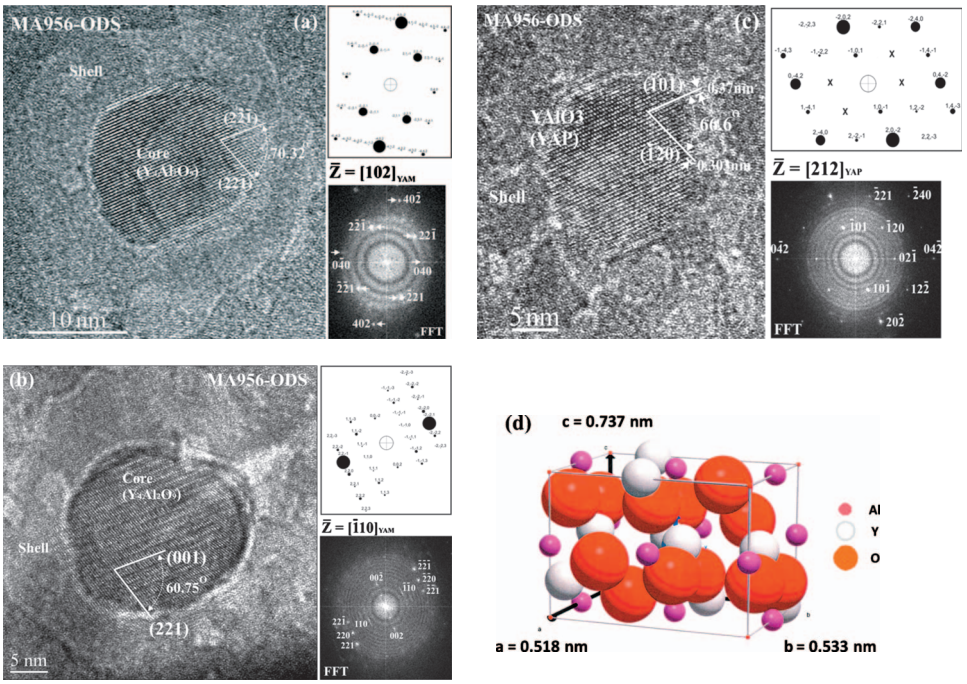

FIG. 16. (Color) HRTEM images show three oxide nanoparticles ($d>20$ nm) with a core/shell structure formed in MA956-ODS. The nanoparticles contain (a) a $Y_4Al_2O_9$ core of the [102] zone, (b) a $Y_4Al_2O_9$ core of the [$\bar{1}$10] zone, (c) a $YAlO_3$ core of the [212] zone, and (d) crystal structure of Y_2AlO_3 (YAP) oxide compound. Here FFT images are shown together with simulated diffraction patterns.

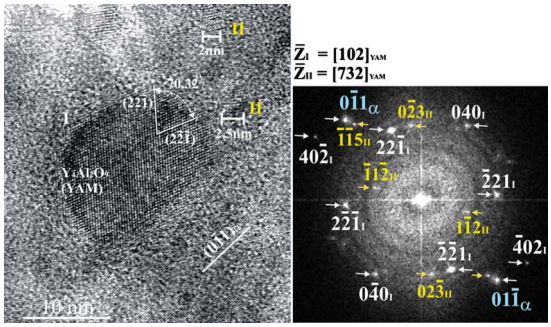

FIG. 17. (Color online) HRTEM image shows a large $Y_4Al_2O_9$ nanoparticle ($d \approx 15$ nm) of the $[102]_I$ zone and two small $Y_4Al_2O_9$ nanoparticle ($2 < d < 3$ nm) of the $[732]_{II}$ zone, which contain no core/shell structure, formed in MA956-ODS. Note that the $Y_4Al_2O_9$ nanoparticle of 2 nm is the smallest crystalline nanoparticle that has been observed using HRTEM techniques.

number of helium atoms (N_g) in each cavity, according to the rate theory of swelling in irradiated metals.[28,29] The increase in both S and N_g in the high-energy neutron damage environment of fusion reactors can result in the decrease in the critical cavity radius above which rapid vacancy- or bias-driven growth occurs and leads to cavitational swelling. When the number of helium atoms within a cavity exceeds a critical value (n_g^*), the critical radius effectively disappears and bias-driven cavity growth occurs regardless of the cavity radius. The size for which the critical radius disappears upon the addition of more helium is termed the minimum critical radius (r_c^*). The helium-filled cavities with radii larger than r_c^* are called voids; the helium-filled cavities with radii smaller than r_c^* are called helium-inflated cavities or helium bubbles. It is noteworthy that theoretically the critical cavity radius containing no helium gas (r_c^0) is about 1.5 times of the critical cavity radius containing helium gas (r_c^*),[28] which has been empirically determined to be 2.5 nm (i.e., $d_c^*=5$ nm) in an Fe-10 Cr alloy that was implanted with 300 ppm helium, annealed, and then ion irradiated to 30 dpa at 574 °C.[30]

A crucial concept (hypothesis) of developing ODS steels for radiation tolerance or swelling resistance is that the onset of swelling can be effectively delayed by the formation of a high density of helium-filled cavities at a fine dispersion of nanoscale particles to reduce the number of helium atoms for each cavity to below the critical number of helium atoms (n_g^*) thus inhibiting rapid void growth. The reasons of achieving this effect can be twofold. First, an increase in cavity density leads to an increase in n_g^* and r_c^* because the excess vacancy flux (S) to each cavity is reduced. The second reason is that an increase in cavity density can reduce the accumulation rate of helium atoms in each cavity since the number of helium atoms available is diluted over a large number of cavities. Thus, the helium concentration, which can be accommodated without swelling, is greater in ODS steels than in a non-ODS matrix of the same alloy composition. A cavity number density higher than 5×10^{12} m^{-3} was accordingly postulated by Mansur and Lee[31] to be one of the principles for alloy design to achieve swelling resistance. According to their theoretical calculations, $\sim 7.5 \times 10^3$ appm helium can be accommodated without triggering swelling when the cavity number density is 5×10^{12} m^{-3}. It is noteworthy that for an assumed plant lifetime of 30 years, $\sim$750 dpa and $\sim 7.5 \times 10^3$ appm helium will be produced in the first wall of a fusion reactor.[32] The existence of critical quantities of r_c^* and n_g^* for bubble-to-void conversion leads to the expectation of a bimodal size distribution of cavities. That is, some cavities containing more than n_g^* helium atoms grow more rapidly to larger voids, and other cavities containing less than n_g^* helium atoms remain as small and stable bubbles. A bimodal size distribution of cavities was accordingly observed in irradiated Fe-Cr ferritic alloys containing a low number density ($< 1 \times 10^{21}$ m^{-3}) of oxide particles or no oxide particles,[30,33,34] and a unimodal size distribution of cavities was observed in irradiated ODS

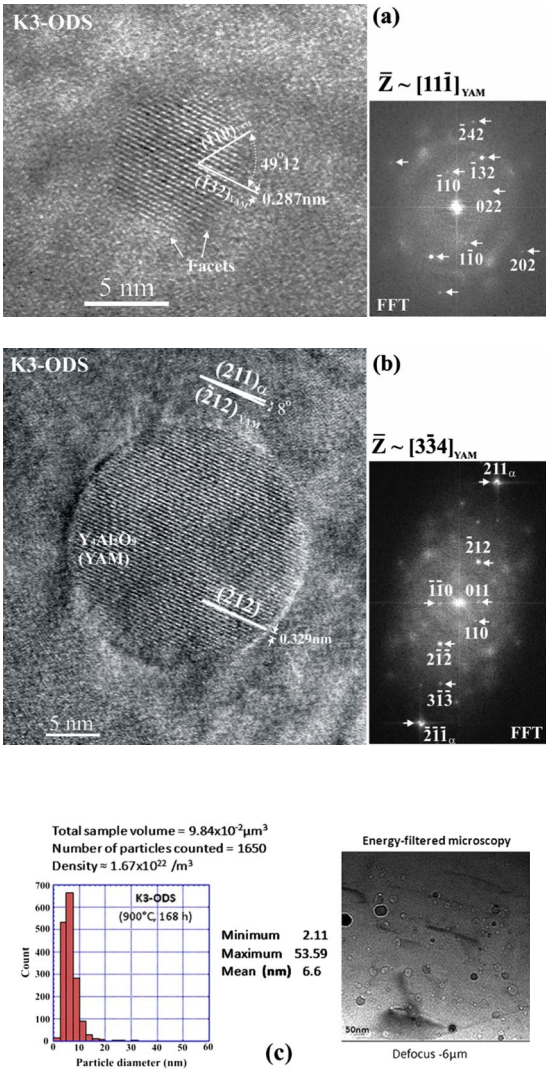

FIG. 18. (Color online) HRTEM images show (a) a small $Y_4Al_2O_9$ nanoparticle (<10 nm), viewed from the $[11\bar{1}]$ direction, remains facetted, (b) a large $Y_4Al_2O_9$ nanoparticle (>20 nm), viewed from nearly the $[3\bar{3}4]_{YAM}$ zone, becomes perfectly spherical without a core/shell structure in K3-ODS steel after annealing at 900 °C for 168 h, and (c) the number density, the size distribution, and the mean size of oxide nanoparticles are displayed together with a typical morphology of nanoparticles observed using energy-filtered microscopy.

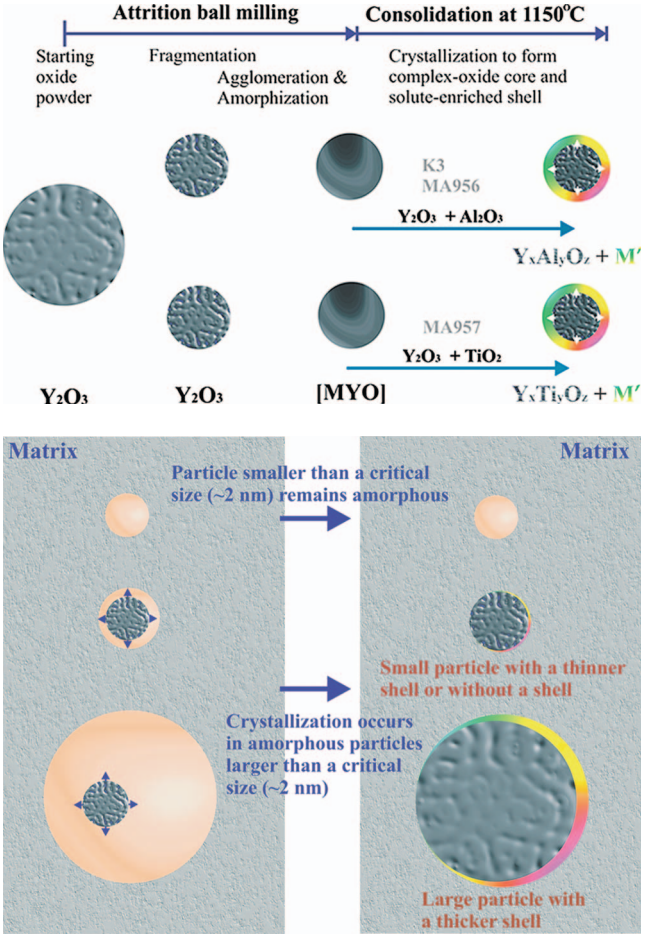

FIG. 19. (Color) Schematic illustrations show (a) a three-stage mechanism for the formation of oxide nanoparticles containing a core/shell structure during MA and consolidation (b) size effect on the formation of core/shell structures in oxide nanoparticles. A solute-enriched shell can form in particles larger than 2 nm when solute depletion rate from the core is greater than solute diffusion rate from the oxide/matrix interface during the crystallization stage; a particle smaller than 2 nm remains amorphous.

steels containing a high number density ($>1\times10^{23}$ m^{-3}) of oxide particles.[33]

To reveal the effect of nanoparticles on the distribution natures of cavities and the role nanoscale crystalline-oxide particles and amorphous clusters in trapping the helium-filled cavities, ($Fe^{8+}+He^{+}$) dual-ion irradiation experiments were conducted on both K3-ODS steel and Fe-14Cr alloy. Effort was made to observe and image the cavities using TEM imaging techniques under out-of-focus (defocus) conditions. Cavities appear as white dots surrounded with a dark Fresnel fringe in underfocus images and as dark dots surrounded with a bright Fresnel fringe in overfocus images.[35] Important results including HRTEM observations are demonstrated and critically discussed below.

1. Fe-14Cr

Figure 20(a) shows a typical TEM observation of cavities formed in irradiated Fe-14Cr, which have diameters ranging between 0.9 and 15 nm and a number density of ~1.7

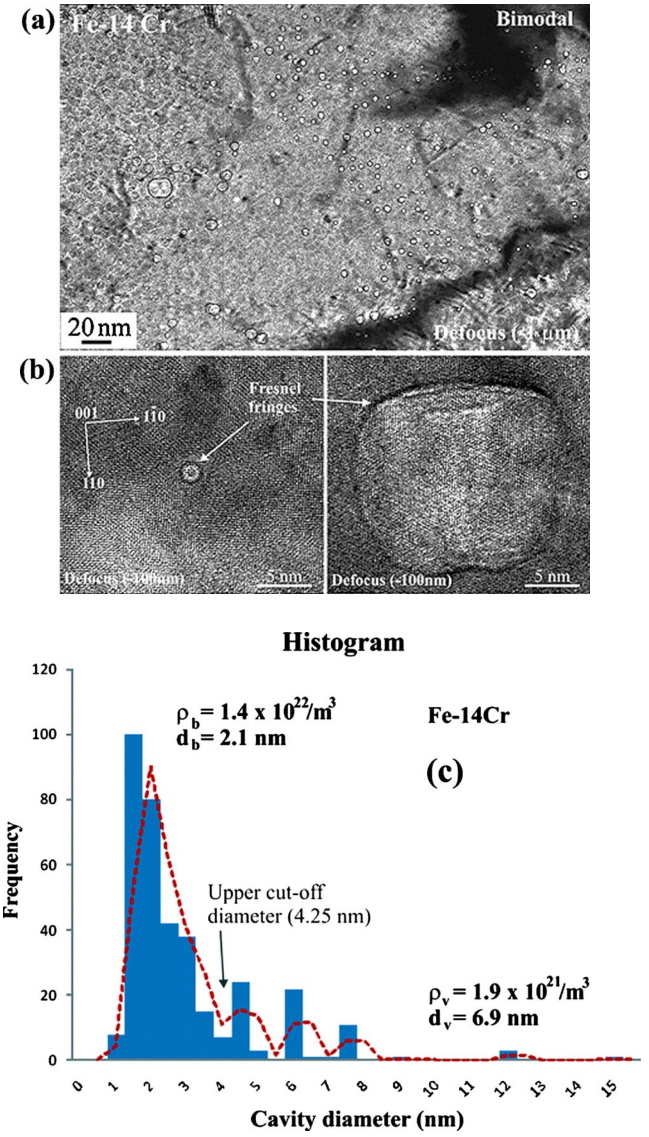

FIG. 20. (Color online) (a) Bright-field TEM image, (b) HR-TEM images, and (c) histogram of cavity diameters versus frequency show a bimodal distribution of cavities in irradiated Fe-14Cr.

$\times10^{22}$ m^{-3}. Notice that the distribution of cavities is somewhat uneven and localized. Figure 20(b) shows HRTEM images of a spherical cavity of a diameter of ~2 nm and an imperfect faceted cavity of a diameter of ~15 nm. Both cavities are surrounded by a dark Fresnel fringe in an underfocus condition of −100 nm. Figure 20(c) is a histogram of cavity diameter versus frequency, which clearly reveals a bimodal distribution of cavities in irradiated Fe-14Cr. The larger cavities (voids) have a density population (ρ_v) of 1.9×10^{21} m^{-3} and an average diameter (d_v) of 6.9 nm. The smaller cavities (bubbles) have a number density (ρ_b) of 1.5×10^{22} m^{-3} and an average diameter (d_b) of 2.1 nm. Here the upper cut-off diameter for the smaller cavities is ~4.25 nm, which is approximately equal to the theoretical minimum critical diameter ($2r_c^*$) above which bias-driven growth occurs. Thus, assuming that the smaller cavities have not achieved the critical radius and the larger cavities have

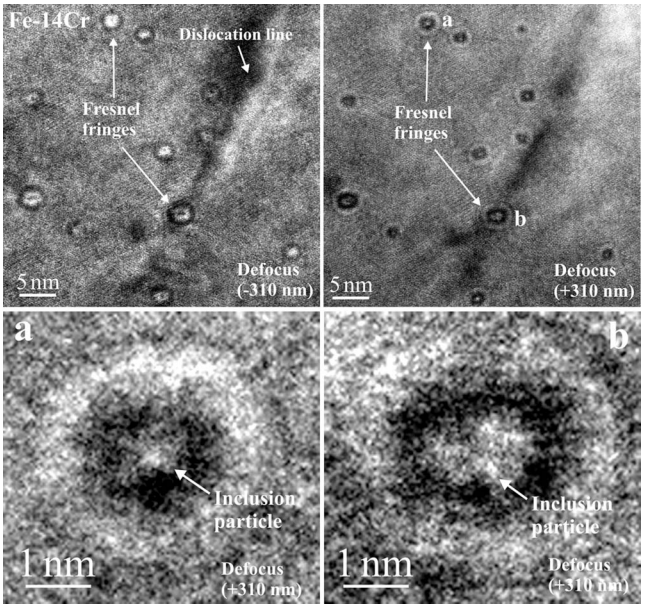

FIG. 21. Bright-field TEM images show the heterogeneous nucleation of helium bubbles in association with dislocation lines and inclusion particles. The high-magnification TEM images taken from the bubbles labeled a and b reveal that inclusion particles of ~1 and ~2 nm can be readily seen within these two bubbles, which appear as black contrasts surrounded by a white Fresnel fringe in overfocus images.

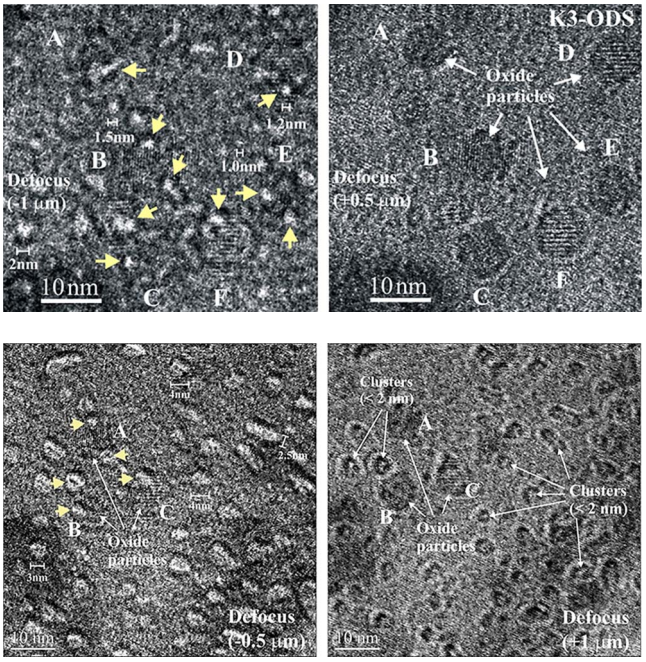

FIG. 22. (Color online) TEM images show (a) many spherical cavities ($d=1-2$ nm), which are mostly located at the oxide/matrix interfaces, can be clearly seen in under an underfocus condition: -1 μm; the crystalline-oxide particles appeared with lattice fringes (labeled A through F; $d=5-10$ nm) can be more readily seen under an overfocus condition of +0.5 μm; (b) the formation of cavities in association with crystalline-oxide particles (labeled A, B, C; $d \approx 10$ nm) and clusters ($d<2$ nm), both can be more readily seen under an overfocus condition of +0.5 μm.

exceeded the critical radius, the critical radius of cavity (r_c^*) estimated from the experimental data shown in Fig. 20(c) is ~2.1 nm. This is reasonable compared to the value ($r_c^* \approx 2.5$ nm) reported for Fe-10Cr irradiated at 574 °C.[30] It is noteworthy that cavities with a size smaller than $r_c^0(=1.5r_c^* \approx 3.15$ nm) or $d_c^0(=2r_c^0 \approx 6.3$ nm) cannot survive without becoming inflated by helium gas. Thus, the observed cavities shown in Figs. 20(a) and 20(b) are in fact helium-inflated cavities, i.e., helium bubbles. It is also noteworthy that many small bubbles tend to form heterogeneously with dislocation lines and inclusion particles, as shown in Fig. 21. Here, as more clearly shown in two high-magnification images of the bubbles marked by a and b, inclusion particles of ~1 and ~2 nm can be seen within these two bubbles that appear as black contrasts surrounded with a white Fresnel fringe in overfocus images. The heterogeneous nucleation of cavities at dislocation lines and inclusion particles leads to the uneven and localized distribution of cavities in irradiated Fe-14Cr.

2. K3-ODS

A typical TEM observation of a unimodal distribution of cavities in irradiated K3-ODS is shown in Fig. 22. Many spherical cavities ($d=1-2$ nm), which are mostly located at the oxide/matrix interfaces, can be clearly seen in Fig. 22(a) under an underfocus condition of -1 μm. The crystalline-oxide particles, which appear with lattice fringes (labeled A through F; $d=5-10$ nm), can be more readily seen in Fig. 22(a) under an overfocus condition of +0.5 μm. Figure 22(b) shows the formation of cavities in association with crystalline-oxide particles (labeled A, B, C; $d \approx 10$ nm) and clusters ($d<2$ nm), both can be more readily seen under an overfocus condition of +0.5 μm. The cavities in association with cluster cores can have nearly spherical, platelet, or cuboidal shape depending on the shapes of the clusters. Those nearly spherical cavities, which contain spherical clusters ($d<2$ nm), have an apparent size: 3–4 nm in diameter. Those platelet cavities (~2.5 nm thick) contain platelet clusters that are thinner than 2 nm. Since almost all the observed cavities have sizes smaller than r_c^0(~3.15 nm) or d_c^0(~6.3 nm), they can be called helium-inflated cavities or helium bubbles. High-resolution TEM images of helium bubbles in association with cluster domains of various shapes are shown in Fig. 23(a). Here each helium bubble appears as white contrast surrounded with a dark Fresnel fringe in the underfocus image. Also noted is that each helium bubble appears as a thin "shell" "encompassing" feature of helium surrounding the disordered (amorphous) cluster domain. The possible formation mechanism of this helium structure may be visualized by examining Fig. 23(b), in which several individual bubbles are found to trap at a cluster domain. This suggests that the appearance of cluster core/bubble shell is a result of the coalescence of small bubbles (or helium-vacancy clusters) trapped at a disordered cluster domain, as conceptualized in the illustration in Fig. 23(b).

Note that the cavity number density in irradiated K3-ODS (Fig. 21) is $\sim 2.0 \times 10^{23}$ m^{-3}, which is an order of magnitude higher than both the number density of crystalline-oxide

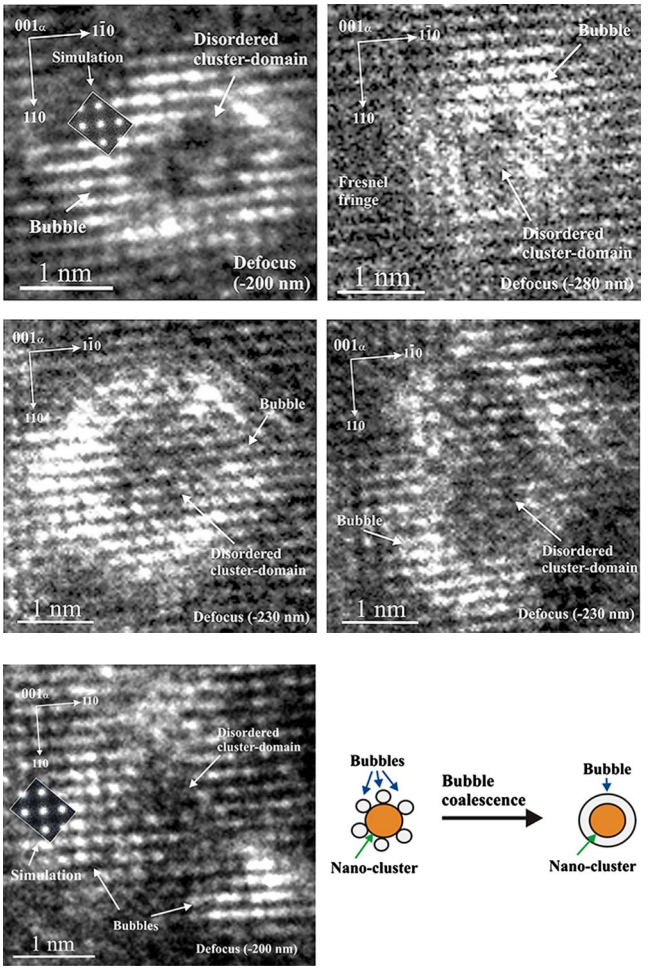

FIG. 23. (Color online) (a) HRTEM images of helium bubbles in association with cluster domains of various shape. Here each helium bubble appears as white contrast surrounded by a dark Fresnel fringe in each underfocus image; (b) HRTEM image shows the trapping of several individual bubbles at a disordered cluster domain, which suggests that the appearance of cluster core/bubble shell is a result of the coalescence of small bubbles as conceptualized in the illustration.

nanoparticles of $\sim 1.0\times 10^{22}$ m^{-3} (Fig. 3) and the cavity number density of $\sim 2.0\times 10^{22}$ m^{-3} in irradiated Fe-14Cr (Fig. 20). This suggests that the helium-filled cavities (bubbles) in irradiated K3-ODS were mostly trapped at amorphous nanoclusters ($d<2$ nm), which are difficult to resolve using conventional TEM imaging techniques. The K3-ODS steel is considered to be swelling resistant since the cavity number density in irradiated K3-ODS is greater than the critical number density of 5×10^{22} m^{-3} for alloy design to achieve swelling resistance.[31] The high-density amorphous nanoclusters may be playing a dominant role by virtue of their high number density in enhancing the radiation tolerance of ODS steels with respect to helium management of the attainable helium atoms for each cavity to below critical quantity of n_g^* for swelling.

IV. CONCLUSION

The crystal structure, the number density, the size distribution, and the interfacial structure of oxide nanoparticles in MA956 and K3 ODS ferritic steels have been investigated. Oxide nanoparticles with a structure characterized by a crystalline core and an amorphous shell were frequently observed in as-fabricated K3 and MA956 ODS steels. The core is mainly $Y_4Al_2O_9$ (YAM) complex oxide. Oxide nanoparticles in K3-ODS steel are denser and finer than those in MA956-ODS steel investigated here. Small crystalline nanoparticles ($d<10$ nm) tend to be coherent or semicoherent with the matrix; large crystalline nanoparticles ($d>20$ nm) tend to be incoherent with the matrix. A three-stage formation mechanism of oxide nanoparticles is proposed: (1) fragmentation of starting Y_2O_3 particles during early stages of ball milling; (2) agglomeration and solid-state amorphization of Y_2O_3 fragments mixing with matrix constituents during later stages of ball milling; (3) crystallization of the amorphous agglomerates larger than ~ 2 nm to form oxide nanoparticles with a core/shell structure during the consolidation at 1150 °C. Agglomerates or clusters smaller than ~ 2 nm remain amorphous (disordered). The core/shell structures of oxide nanoparticles formed in as-fabricated K3 and MA956 ODS steels are far from chemical equilibrium; the core/shell structure of oxide nanoparticles in K3-ODS vanishes after prolonged annealing.

Results of (Fe^{8+}+He^+) dual-ion irradiation experiments reveal the formation of a bimodal and uneven distribution of cavities with a number density of $\sim 2.0\times 10^{22}$ m^{-3} in Fe-14Cr but a unimodal distribution of cavities with a number density of $\sim 2\times 10^{23}$ m^{-3} in K3-ODS. The uneven distribution of cavities in irradiated Fe-14Cr is likely due to the heterogeneous nucleation of cavities at dislocations and inclusion particles, whereas the unimodal distribution of cavities in K3-ODS is likely due to the heterogeneous nucleation of cavities at high number density of nanoclusters ($d<2$ nm). The amorphous nanoclusters are found to play a possible important role in enhancing radiation resistance of K3-ODS steel with respect to helium management of the attainable helium atoms for each cavity to below critical quantity of n_g^* for swelling.

ACKNOWLEDGMENTS

This work was performed under the auspices of the U.S. Department of Energy by Lawrence Livermore National Laboratory under Contract No. DE-AC52-07NA27344. Work at LLNL was funded by the Laboratory Directed Research and Development Program at LLNL under project tracking code 09-SI-003. The author gratefully acknowledges B. El-dasher for supplying Fe-20Cr (MA 956) ODS steel, M. A. Wall for particle-size distribution analyses, and N. E. Teslich and R. J. Gross for TEM sample preparations, R. L. Krueger for the design of sample holder for irradiation.

*Corresponding author. FAX: +1-925 424 3815; hsiung1@llnl.gov

[1] K. Ehrlich, Philos. Trans. R. Soc. London, Ser. A **357**, 595 (1999).
[2] E. E. Bloom, S. J. Zinkle, and F. W. Wiffen, J. Nucl. Mater. **329-333**, 12 (2004).
[3] S. Ukai and M. Fujiwara, J. Nucl. Mater. **307-311**, 749 (2002).
[4] A. Kohyama, M. Seki, K. Abe, T. Muroga, H. Matsui, S. Jitsukawa, and S. Matsuda, J. Nucl. Mater. **283-287**, 20 (2000).
[5] E. E. Bloom, J. T. Busby, C. E. Duty, P. J. Maziasz, T. E. McGreevy, B. E. Nelson, B. A. Pint, P. F. Tortorelli, and S. J. Zinkle, J. Nucl. Mater. **367-370**, 1 (2007).
[6] J. Boutard, A. Alamo, R. Lindau, and M. Rieth, C. R. Phys. **9**, 287 (2008).
[7] T. Tanaka, K. Oka, S. Ohnuki, S. Yamashita, T. Suda, S. Watanabe, and E. Wakai, J. Nucl. Mater. **329-333**, 294 (2004).
[8] E. E. Bloom, J. Nucl. Mater. **85-86**, 795 (1979).
[9] K. Yutani, H. Kishimoto, R. Kasada, and A. Kimura, J. Nucl. Mater. **367-370**, 423 (2007).
[10] R. Kasada, N. Toda, K. Yutani, H. S. Cho, H. Kishimoto, and A. Kimura, J. Nucl. Mater. **367-370**, 222 (2007).
[11] S. Ukai, T. Nishida, H. Okada, T. Okuda, M. Fujiwara, and K. Asabe, J. Nucl. Sci. Technol. **34**, 256 (1997).
[12] S. Ukai, T. Nishida, T. Okuda, and T. Yoshitake, J. Nucl. Sci. Technol. **35**, 294 (1998).
[13] C. Boudias and D. Monceau, The crystallographic software for research and teaching, Senlis, France, 1989–1998.
[14] A. N. Christensen and R. G. Hazell, Acta Chem. Scand., Ser. A **45**, 226 (1991).
[15] W. Y. Ching and Y. N. Xu, Phys. Rev. B **59**, 12815 (1999).
[16] V. de Castro, T. Leguey, M. A. Monge, A. Muñoz, R. Pareja, D. R. Amador, J. M. Torralba, and M. Victoria, J. Nucl. Mater. **322**, 228 (2003).
[17] T. Okuda and M. Fujiwara, J. Mater. Sci. Lett. **14**, 1600 (1995).
[18] Y. Kimura, S. Takaki, S. Suejima, R. Uemori, and H. Tamehiro, ISIJ Int. **39**, 176 (1999).
[19] H. Sakasegawa, M. Tamura, S. Ohtsuka, S. Ukai, H. Tanigawa, A. Kohyama, and M. Fujiwara, J. Alloys Compd. **452**, 2 (2008).
[20] M. J. Alinger, G. R. Odette, and D. T. Hoelzer, Acta Mater. **57**, 392 (2009).
[21] L. S. Darken and R. W. Gurry, *Physical Chemistry of Metals* (McGraw-Hill, New York, 1953).
[22] L. Wen, X. Sun, Z. Xiu, S. Chen, and C.-T. Tsai, J. Eur. Ceram. Soc. **24**, 2681 (2004).
[23] E. A. Marquis, Appl. Phys. Lett. **93**, 181904 (2008).
[24] M. Klimenkov, R. Lindau, and A. Möslang, J. Nucl. Mater. **386-388**, 553 (2009).
[25] L. L. Hsiung, M. J. Fluss, and A. Kimura, Mater. Lett. **64**, 1782 (2010).
[26] T. Koyano, T. Takizawa, T. Fukunaga, U. Mizutani, S. Kamizuru, E. Kita, and A. Tasaki, J. Appl. Phys. **73**, 429 (1993).
[27] C. Suryanarayana, Prog. Mater. Sci. **46**, 1 (2001).
[28] L. K. Mansur and W. A. Coghlan, J. Nucl. Mater. **119**, 1 (1983).
[29] L. K. Mansur, E. H. Lee, P. J. Maziasz, and A. P. Rowcliffe, J. Nucl. Mater. **141-143**, 633 (1986).
[30] L. L. Horton and L. K. Mansur, ASTM Spec. Tech. Publ. **870**, 344 (1985).
[31] L. K. Mansur and E. H. Lee, J. Nucl. Mater. **179-181**, 105 (1991).
[32] K. Ehrlich, Fusion Eng. Des. **56-57**, 71 (2001).
[33] T. Yamamoto, G. R. Odette, P. Miao, D. J. Edwards, and R. J. Kurtz, J. Nucl. Mater. **386-388**, 338 (2009).
[34] I.-S. Kim, J. D. Hunn, N. Hashimoto, D. L. Larson, P. J. Maziasz, K. Miyahara, and E. H. Lee, J. Nucl. Mater. **280**, 264 (2000).
[35] M. Ruhle and M. Wilkens, Cryst. Lattice Defects **6**, 129 (1975).